Noise Source Analysis in Counter Rotating Open Rotors

Dale A. Smith * and Antonio Filippone.†
Department of MACE, University of Manchester, M13 9PL, UK.

George N. Barakos‡
CFD Laboratory, University of Glasgow, G12 8QQ, UK.

Due to their potential to reduce aircraft emissions, Counter Rotating Open Rotors (CROR) have seen a renewed interest in applications, from civil aviation to urban air mobility. However, there are concerns surrounding their acoustic emissions. In the work presented, we investigated the noise sources for a range of CROR configurations for a general aviation class aircraft. Numerical models are used to compute the aerodynamic and aeroacoustic performance of these configurations. Further dissection of the various CROR noise sources is then carried out in order to better understand their contribution to CROR noise, and to direct the design of future low-noise CROR. Noise reductions were observed when the rotor-rotor spacing was increased. Increased contraction of the wake requires the need for increased clipping to reduce the tip vortex interaction source. Noise reductions were also observed in the case of asynchronous rotational speeds. However, this was accompanied by a reduction in propulsive efficiency. Analysis of the CROR in non-axial flight demonstrated the need to evaluate noise-reducing strategies at off-design conditions. Whilst the analysis proved the ability to reduce various CROR noise sources, it highlighted that trade-offs with aerodynamic performance is necessary.

Nomenclature

CROR	=	Counter Rotating Open Rotor
SPL	=	Sound Pressure Level
TVI	=	Tip Vortex Interaction
c	=	Blade element chord
c_0	=	Speed of sound
$\boldsymbol{F}_i/\boldsymbol{F}_v$	=	Vector of inviscid/viscous fluxes
g	=	Axial distance between rotors

*Research Assistant, Department of MACE, The University of Manchester, M13 9PL, UK
†Professor, Department of MACE, The University of Manchester, M13 9PL, UK, Senior AIAA Member.
‡Professor, School of Engineering, University of Glasgow, G12 8QQ, UK

k	=	Scattering index
M	=	Mach number
M_n	=	Mach number in normal direction
M_r	=	Mach number in radiation direction
M_T	=	Tip Mach number
$\boldsymbol{n}$	=	Unit normal
N	=	Blade count
p'	=	Acoustic pressure
p_s	=	Blade surface pressure
Q	=	Torque
r_h	=	Hub radius
R	=	Tip radius
$\boldsymbol{R}$	=	Vector of flux residuals
$\mathcal{R}$	=	Source-observer distance
$\boldsymbol{S}$	=	Source term accounting for rotor rotation
S	=	Blade surface
t	=	Observer time
t/c	=	Thickness-chord ratio
T	=	Thrust
u, v, w	=	Cartesian velocity components
$\mathcal{V}$	=	Control Volume
$\mathcal{V}$	=	Cell volume
V_∞	=	Free stream velocity
$\boldsymbol{W}$	=	Vector of conserved variables
$\boldsymbol{x}$	=	Observer location
α	=	Angle of rotor disc
η	=	Propulsive efficiency, $V_\infty T/\Omega Q$
θ	=	Polar flyover angle
Θ	=	Angle between normal and radiation direction
ρ	=	Fluid density
σ	=	Blade solidity, $Nc/\pi R$
τ	=	Source time

ψ = Azimuth angle

Ω = Rotational speed

$[\cdot]_{1,2}$ = Fore/aft rotor

I. Introduction

Counter Rotating Open Rotors (CROR) are once again seeing a renewed interest due to their potential to reduce aircraft fuel consumption in a time where the aviation industry is facing increased pressure to reduce emissions. Comprised of two open blade rows, the counter rotation of the aft row (relative to the fore) removes residual swirl from the flow and subsequently improves propulsive efficiency. Furthermore, the high bypass ratio and the absence of a duct allows the CROR to offer significant reductions in fuel consumption and emissions relative to modern turbofan architectures [1].

Despite their potential to reduce aircraft emissions, without a duct to limit noise propagation, CROR noise still poses a challenge for the propulsion system. CROR noise evaluation is a complex problem, owing to the fact that CROR noise is highly tonal, with significant amplitudes along most directivities [2, 3] and through a wide frequency range [4].

CROR noise can be characterised in the same way as the single rotation propeller. It is comprised of the steady loading, thickness, and for high tip speeds, quadrupole sources [5]. However, CROR noise is further complicated through the addition of the unsteady noise sources which arise due the unsteady interaction between fore and aft blade rows. From Figure 1, the potential field of the aft rotor results in periodic unsteady loading on the fore rotor. Similarly, the potential field from the fore rotor results in periodic unsteady loading on the aft rotor. The rear rotor will also have additional periodic loading as it cuts through the wake and tip vortices from the fore rotor.

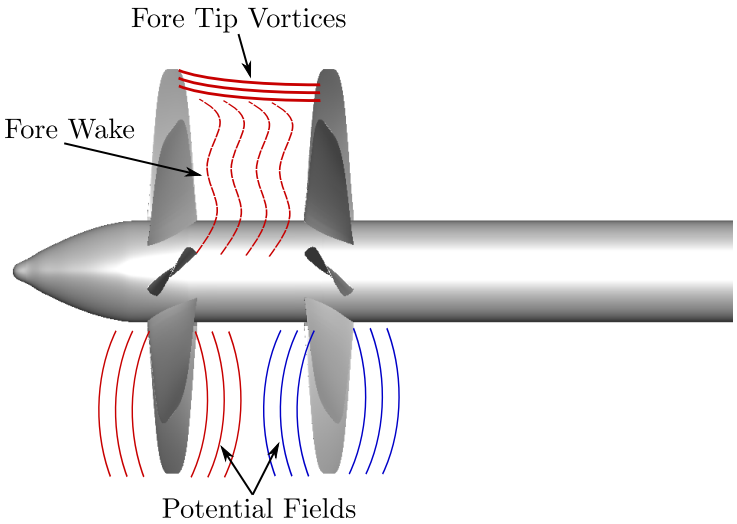

Fig. 1 *CROR interaction sources.*

The focus of recent work on CROR noise has concentrated on modifications of the fore rotor wake in order to reduced the interactions with the aft rotor. However, earlier work involving the Fairey Gannet [6, 7] demonstrated the importance of the potential field interactions, particularly for the unsteady loading on the fore rotor. Furthermore, recent work by the present authors [8] also showed the importance of the upstream interactions. These results showed that with

low-solidity blade designs the upstream interactions were as important as the downstream interactions.

The installation of the CROR on the aircraft has also been found to introduce further unsteady interaction sources, in particular for pylon mounted configurations [9–11]. Furthermore, similarly to the isolated rotor case, CROR at non-axial flight also give rise to additional unsteady loading components which can further increase the noise [12]. Finally, the broadband noise has also been shown to be an important source in the total CROR noise emissions [13, 14]

While there have been a number of novel concepts to reduce CROR noise, careful selection of the more conventional design parameters can be used to reduce the noise. For example, Hanson [15, 16] showed that the CROR noise emissions are strongly coupled to the fore and aft blade counts and tip speeds. With the potential and wake interactions decay increasing with distance between rotors. Therefore, the axial spacing between fore and aft rotors is also an important parameter for both the aerodynamic and aeroacoustic performance of CROR [17].

The effect of various design parameters are typically studied through parametric studies. For large design spaces these are typically carried out using lower-order methods. For example, Parry & Vianello [18] studied the effect of fore and aft blade count and rotational speed combinations on the resulting CROR noise. A similar study was carried out by Smith *et al.* [19] which was furthered with an optimisation study of the blade counts and tip speeds. In both studies it was shown that careful selection of blade counts and tip speeds could be used to reduce the interaction and the subsequent noise emissions. Both studies showed that the CROR follows the same relationship as the isolated rotor where lower tip speeds and larger blade counts are favourable for reduced noise. Smith *et al.* [20] performed a parametric study of the effect of the blade count when either fore or aft blade row was locked to reduce noise. Whilst the authors demonstrated that the noise could be reduced through locking a blade row, ultimately the lowest noise was found for a CROR with the greatest blade count combination.

Woodward [21] performed an experimental parametric study of the spacing between blade rows. Woodward showed that increased spacing had a beneficial impact on the CROR noise. However, with increased spacing the tip vortex from the fore rotor moves inboard, and as a result, there may be an increase in the Tip Vortex Interaction (TVI) noise source. To address the TVI source, clipping of the aft rotor is often utilised [22, 23]. Woodward & Gordon [24] showed that the clipped aft rotor was more sensitive to the spacing changes. Furthermore, Dittmar [25] showed that clipping could be made redundant for particular rotor loading and axial spacing combinations. Additionally, the issue is compounded due to the fact that the fore rotor wake decays more rapidly than the tip vortices. As a result, for low values of spacing the wake dominates, and as the spacing increases, the TVI source dominates [26]. Considering all this, combinations of clipping and axial spacing must be investigated over a range of operating points in order to ensure the clipping is most optimally utilised over the flight envelope [27].

The effect of design parameters can also be investigated through optimisation studies. For example, Peters & Spakovszky [28] carried out an optimisation of a CROR with particular focus on the interaction mechanisms. They demonstrated significant noise reductions relative to a baseline design through increased clipping and rotor spacing. Grasso *et al.* [29] carried out an optimisation of a CROR to simultaneously minimise noise and maximise aerodynamic performance. Whilst the authors found that the aerodynamic and aeroacoustic objectives to be competing, they identified designs which could meet both objectives. In particular, they identified designs with increased spacing and reduced blade chords. Lepot *et al.* [30] and Schnell *et al.* [22] presented work from a European-wide project investigating the optimisation of CROR configurations. In particular, they used high-order methods coupled to an evolutionary algorithm to investigate a range of design variables that minimised noise at take-off and maximised efficiency at top of climb.

They found that the objectives could be met with modifications to the blade profile shapes and by offloading the front rotor to reduce the wake deficit impacting the rear rotor which itself benefited from clipping.

In this contribution, we utilise high-fidelity methods to investigate a number of CROR design features and their effects on the resulting noise emissions. In particular, we aim to exploit acoustic tools in order to isolate the tonal noise sources (with the broadband components being neglected at present), to evaluate their contribution to the total noise emissions of the isolated CROR. The findings from these investigations will then direct future work to target noise reductions of the interaction component early in the design of a low noise CROR. In the investigation, we consider four configurations that will highlight the role of the interaction component on some common CROR design and operational parameters. For each configuration, all design parameters are the same, except the parameter of interest. All configurations have the same fore and aft blade count. The focus of the present study is on applications to general aviation aircraft. However, the work may have further application in the design of CROR for urban air mobility, which use similar low-solidity rotor designs.

II. Description of Test Cases

With the aim of investigating the interaction noise of CROR, four configurations have been studied: (i) baseline configuration; (ii) non-zero incidence angle; (iii) non-equal rotational speed; and (iv) increased rotor-rotor spacing.

Using the FLIGHT aircraft performance code [31, 32] to simulate a representative general aviation aircraft, the baseline CROR was sized to deliver a required take-off thrust of $T = 6$ kN at $M_\infty = 0.2$. With equal fore and aft blade counts ($N_1 = N_2 = 4$) and tip speeds ($M_T = 0.46$), corresponding to $\Omega = 1,000$ rev/min, a 3m diameter CROR design resulted. Table 1 shows the pertinent design features of the baseline configuration. Note that fore and aft rotors are of equal diameter, i.e. no clipping. Whilst clipping is commonly used to reduce CROR noise, in the present study we are interested in investigating the effect of various design changes on this source. The blades of all configurations are of SR2 design, Figure 2.

The baseline configuration considers a simplified analysis at take-off where the rotors are considered in axial flight. However, under more realistic conditions, the rotors will see a large variation in incidence angles. Therefore, the noise of the CROR is studied at non-axial flight conditions. In particular, the baseline configuration is studied at a rotor incidence angle of $\alpha = 5°$.

The baseline configuration, with equal blade counts and rotational tip speeds, perhaps represents an acoustically sub-optimal configuration. With the equal blade counts and tip speeds resulting in high acoustic interaction between fore and aft rows (constructive addition of acoustic waves). To overcome this, either unequal blade counts or unequal rotational speeds may be used. Unequal fore and aft rotational speeds were chosen due to the simplicity of running the simulation. Whilst for unequal blade counts, the blades would have to be scaled to ensure equal blade loading per unit blade area and hence require additional grids to be generated. The unequal rotational speed allows for simple changes in the simulation input files. For the present case, the fore rotor rotational speed was increased to 1,050 rev/min, whilst the aft rotor rotational speed was reduced to 945 rev/min. These values were chosen to simplify the post-processing of the simulation data. Nonetheless, additional processing of the data is required to handle the non-periodic data.

Finally, the baseline configuration is considered with increased spacing between fore and aft blade rows. As the decay of potential fields and rotor wakes will vary with the distance between rotors, the axial spacing is, therefore, an important design choice. Whilst increasing the spacing will result in weaker wake and potential interactions, the

increased distance will result in the tip vortex of the fore rotor impinging in a more inboard region of the aft rotor (as the wake contracts with distance) and may result in a greater source from this contribution. In the present case, the spacing has been increased from its baseline value by 15%, i.e. $g/D = 0.46$.

For all configurations, the required thrust was achieved by adjusting the blade setting angle of fore and aft rotors. The distribution of thrust or torque between fore and aft rotors is an active design choice. The torque ratio defines the design of the power turbine or the gearbox for direct-drive and geared-drive architectures respectively. A number of previous studies have assumed an equal thrust or torque ratio in order to have the total thrust split equally across both rotors [33–35]. However, in some cases this may result in unequal aerodynamic loading. For example, if the aft rotor is clipped [36]. A number of investigations have also used non-equal thrust or torque ratios [37, 38]. Delattre *et al.* [2], in fact, showed that the torque ratio had a significant effect on the resulting noise emissions by offloading one of the rotors. In the present study, we have specified an equal thrust loading on fore and aft rows. This was chosen to simplify the acoustic analysis, where differences in noise levels between fore and aft rotors would not result from differences in the thrust produced by each row.

Table 1 *Baseline design parameters.*

Parameter	σ	$R_1 = R_2$ [m]	r_h/R	g/R	$M_{T_1} = M_{T_2}$
Value	0.36	1.5	0.24	0.4	0.46

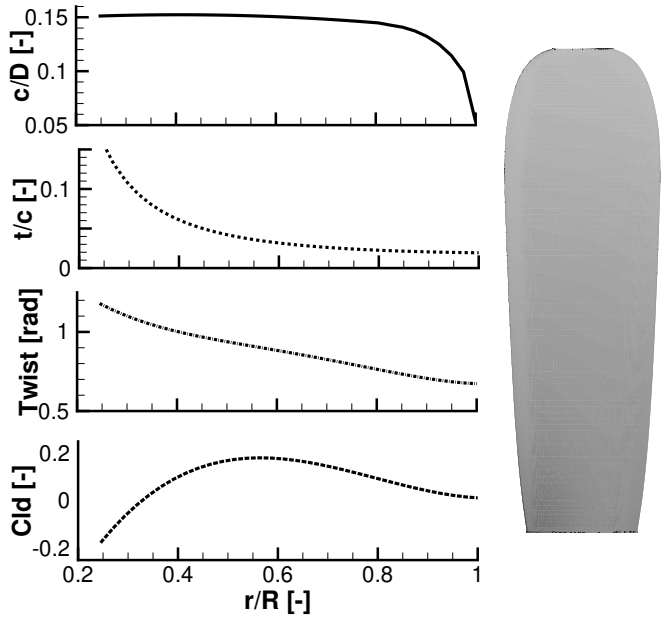

Fig. 2 *SR2 blade geometry.*

III. Computational Model

A. The HMB Solver and CFD Simulation

The Helicopter Multi Block HMB3 solver [39, 40] was used to perform unsteady Reynolds Averaged Navier-Stokes (uRANS) CFD simulations throughout this work. HMB3 solves the uRANS equations in dimensionless, integral form using the arbitrary Lagrangian-Eulerian [41] formulation for time-dependent domains with moving boundaries:

$$\frac{\mathrm{d}}{\mathrm{d}t}\int_{\mathcal{V}(t)} \boldsymbol{W}\,\mathrm{d}\mathcal{V} + \int_{\partial\mathcal{V}(t)} (\boldsymbol{F}_i(\boldsymbol{W}) - \boldsymbol{F}_v(\boldsymbol{W}))\cdot\boldsymbol{n}\,\mathrm{d}S = \boldsymbol{S} \tag{1}$$

$\mathcal{V}(t)$ is the time-dependent control volume, with $\partial\mathcal{V}(t)$ its boundary; $\boldsymbol{W}$ is the vector of conservative variables, $[\rho, \rho u, \rho v, \rho w, \rho E]^T$; $\boldsymbol{F}_i$ and $\boldsymbol{F}_v$ are the inviscid and viscous fluxes respectively; $\boldsymbol{n}$ is the unit normal vector pointing outwards and $\boldsymbol{S}$ is the source term. HMB3 offers several uRANS turbulence models to close the viscous stress tensor, including the k-ω SST model [42] which was used throughout this work.

HMB3 discretises the Navier-Stokes equations using a cell-centred finite volume approach on a multi-block grid. This is done on a curvilinear coordinate system, and leads to the following set of equations to solve:

$$\frac{\mathrm{d}}{\mathrm{d}t}(\boldsymbol{W}_{i,j,k}\forall_{i,j,k}) + \boldsymbol{R}_{i,j,k} = 0 \tag{2}$$

$\boldsymbol{W}_{i,j,k}$ is the vector of conserved variables of each cell, with $\forall_{i,j,k}$ the cell volume; $\boldsymbol{R}_{i,j,k}$ is the vector of flux residuals.

Osher's upwind scheme [43] is used to evaluate convective fluxes. Second-order finite differencing is employed to discretise the viscous fluxes. The MUSCL variable extrapolation method [44] is used to provide second-order accuracy in space. A van Albada limiter [45] is used in areas of high-pressure gradients to remove spurious oscillations. An implicit dual time-stepping method is employed to perform time integration in order to achieve fast convergence. The resulting system of linear equations is solved using the generalised conjugate gradient method with Block Incomplete Lower-Upper (BILU) factorisation [46] as a pre-conditioner. Multi-block grids are used for the HMB3 solver, and hence, allows for parallelisation and distribution of the calculation load over many processors.

The HMB3 solver has been validated for a range of rotor flow cases [47–49]. Furthermore, the authors have previously shown the ability of the HMB3 solver in predicting open rotor flows [8, 50].

B. Aeroacoustic Simulations

The Farassat 1A formulation [51] was implemented to compute the acoustic emissions of each configuration in the present analysis. The Farassat formulation is described by a summation of thickness and loading contributions:

$$p'(\boldsymbol{x},t) = p_L{}'(\boldsymbol{x},t) + p_T{}'(\boldsymbol{x},t) \tag{3}$$

where,

$$4\pi p_T{}'(\boldsymbol{x},t) = \rho c_0 \int_{f=0}\left[\frac{\dot{M}_n}{\mathcal{R}(1-M_r)^2} + \frac{M_n\dot{M}_r}{\mathcal{R}(1-M_r)^3}\right]_{ret}\mathrm{d}S + \rho c_0\int_{f=0}\left[\frac{c_0 M_n(M_r-M^2)}{\mathcal{R}^2(1-M_r)^3}\right]_{ret}\mathrm{d}S \tag{4}$$

and

$$4\pi p_L{}'(\boldsymbol{x},t) = \int_{f=0}\left[\frac{\dot{p}_S\cos\Theta}{c_0\mathcal{R}(1-M_r)^2}+\frac{\dot{M}_r p_S\cos\Theta}{\mathcal{R}(1-M_r)^3}\right]_{ret}\mathrm{d}S+ \int_{f=0}\left[\frac{p_S(\cos\Theta-M_n)}{\mathcal{R}^2(1-M_r)^2}+\frac{p_S\cos\Theta(M_r-M^2)}{\mathcal{R}^2(1-M_r)^3}\right]_{ret}\mathrm{d}S \quad (5)$$

Note that the quadrupole and broadband source have been neglected. Neglecting the quadrupole source is acceptable in the this case thanks to the low tip Mach number for all configurations ($M_T = 0.46$). Moreover, whilst the contribution of the broadband sources have been found to be important in some cases for CROR [13], preliminary tools [14] suggested the tonal component to be more significant in the present case. Therefore, our discussion is limited to the tonal contributions to the CROR noise for each configuration.

The $1/\mathcal{R}$ terms in both thickness and loading sources represent the far-field component, while the $1/\mathcal{R}^2$ terms describe the near-field components. M is the Mach number, with subscripts r and n representing the Mach number in the radiation and normal directions respectively, with $\hat{r}$ and $\hat{n}$ the unit radiation and normal vectors respectively. Θ is the angle between the normal and radiation vectors. $\mathcal{R}$ is the magnitude of the radiation vector, r. Finally, p_S is the pressure on the blade surface, S.

The surface pressure from the blades from both fore and aft rotors are extracted at each azimuthal step in the simulation over an entire rotor revolution. The blade surface pressure and its geometry are extracted and passed to the acoustic emissions code to calculate the loading and thickness contributions to the total rotor noise. The present implementation utilised a source-dominant approach. In particular, the acoustic pressure is solved at a specified source time, τ. The sound will then reach the observer at a time, $t = \tau + r/c_0$. This method will result in unequally spaced observer time for each source. Therefore, an observer time is chosen and each source is interpolated onto this time. Alongside allowing for the integration of all blade sources, the specification of the observer time also allows for the addition of sources from both fore and aft rotors.

The present implementation of the Farassat formulation has previously shown the capability in predicting the noise emission for the particular case of CROR [8, 50], and will therefore not be reproduced here.

In the present analysis, the individual CROR noise sources are isolated in order to investigate their relative contribution to the total noise emissions. The thickness and loading contributions are separated explicitly in the Farassat formulation. The steady loading noise sources are isolated by neglecting the pressure derivative terms ($\dot{p}_s$) in Equation (5). The unsteady component is found from the difference between the total loading and the steady component. For the fore rotor, the unsteady contribution results from the potential interaction from the aft rotor. On the other hand, for the aft rotor, the unsteady loading sources comprises contributions from viscous wake and potential interactions from the upstream fore rotor. The Tip Vortex Interaction (TVI) contributes an additional unsteady source on the aft rotor. To isolate this contribution, the noise sources from the aft rotor were associated with their respective spanwise location of interaction. In particular, noise sources between the 85% span and the blade tip were associated with the TVI source, whilst those sources from the root up to the 85% span were attributed to the wake and potential interaction sources. Whilst the wake and potential interactions will still contribute beyond the 85% position, peak loading was observed to be inboard of this 85% location suggesting these contributions would dominate in this inboard region. Furthermore, it is believed that the TVI source will dominate in the outboard region from investigations of the tip vortex trajectories.

IV. Aerodynamic Analysis

Whilst the present study is focused on the analysis of the noise sources from a number of CROR configurations, it is first important to perform an aerodynamic analysis of each of these configurations. The requirement for the analysis of the aerodynamic performance of each configuration is twofold. Firstly, the aerodynamic data is directly fed to the acoustic solver to perform the acoustic simulations, and some of those aerodynamic features may be used to explain the differences between configurations. Secondly, whilst the configurations will offer differing noise emissions, it is important to examine their aerodynamic performance to determine if this is a trade-off and to evaluate the configuration from a more high-level perspective.

To compare each configuration, both fore and aft rotors were trimmed to deliver a thrust representative of a general aviation class aircraft. The FLIGHT software [31, 32] was used to simulate a general aviation class aircraft which resulted in a required take-off thrust of 6 kN per engine. Furthermore, an equal thrust loading between fore and aft rotors is specified. Fore and aft rotors were trimmed by varying the blade setting angles. Table 2 presents the computed thrust for both fore and aft rotors for each configuration.

Each CROR configuration has been trimmed close to the required thrust with an equal loading on both rotors. Whilst there are small differences between each configuration, the largest deviation from the target value is small, $\sim 3.6\%$. Trimming more closely to the required value could be achieved with finer adjustment of the blade setting angle. However, this would require significant additional computational time. Furthermore, the small differences observed are not expected to be a cause for significant variations in computed noise level between the configurations.

Table 2 *Computed loading and propulsive efficiency for each configuration.*

Case	T_1 [kN]	T_2 [kN]	Q_1 [kNm]	Q_2 [kNm]	η [-]
Baseline	3.06	3.05	−2.50	2.49	0.794
Non-axial	3.04	3.08	−2.45	2.46	0.808
Asynchronous	3.01	3.11	−2.36	2.69	0.785
Increased Spacing	3.09	3.08	−2.50	2.49	0.801

Table 2 also presents the resulting torque and propulsive efficiency for each configuration. With the exception of the asynchronous configuration, all configurations show an almost equal torque ratio between fore and aft rotors. For the asynchronous configuration, a torque ratio of $Q_2/Q_1 \sim 1.14$ is found. The increased torque reaction of the aft row results from the aft rotor having to provide the same thrust at a reduced rotation rate relative to the fore rotor. However, considering the relative rotational speeds of both blade rows, a power ratio of $P_2/P_1 \sim 1.03$ results which is approximately equal to the thrust ratio for this configuration.

The asynchronous configuration has the lowest propulsive efficiency of all four configurations considered. Whilst the fore rotor showed the highest propulsive efficiency of any blade row, the increased torque reaction of the aft row resulted in a lower propulsive efficiency and a subsequent reduction of the total propulsive efficiency relative to the baseline configuration. The change in efficiency is driven by changes in the inflow angles to the blade elements of each rotor. For example, the inflow angle to the fore rotor was found to be reduced relative to the baseline configuration. This reduced inflow angle is primarily driven by the increased rotational speed, and subsequently results in a lower angle of attack and in the present case, an improved lift to drag ratio across the blade. For the aft rotor, the reduced rotational speed results in an increased inflow angle and resulting angle of attack to each blade section, resulting in a decrease in

the blade lift to drag ratio. Further changes to the inflow angle are driven by the induction caused by the interaction between the opposing rotors.

Both non-axial and increased spacing configurations show improved propulsive efficiencies relative to the baseline configuration. With increased propulsive efficiency observed for both fore and aft rotors for these configurations. In both cases, comparisons of the inflow angles show reductions for both fore and aft rotors relative to the baseline. Again, this results in reductions in the local angle of attack seen by each blade element and in the present case, improvements in the lift to drag ratio of each blade. The improvements in lift to drag translate directly to increased thrust capability for the same torque and hence increased propulsive efficiency. For the increased spacing configuration, the greater distance between blade rows results in a greater decay of the wake and potential fields. Subsequently, there is reduced induction on each blade row which results in the reduced inflow angles relative to the baseline case. For the non-axial configuration, the additional velocity components due to the inclination of the disc result in modifications to the inflow to each blade element, in addition to the effects of mutual interaction.

Whilst we have evaluated the propulsive efficiency of each configuration at take-off, it is their value at cruise conditions that is important for the design of CROR. Therefore, each configurations should be re-evaluated under cruise conditions to allow for a better comparison between configurations at typical design objectives, in particular high propulsive efficiency during cruise and low community noise at take-off.

The interaction between fore and aft rotors results in unsteady loading on both rotors, and subsequently the unsteady noise source. To illustrate the unsteady loading observed as the blades rotate, Figure 3 presents the three force components for a single reference blade from both fore and aft rotors for all configurations. The three Cartesian components are defined by the axes shown in Figure 5.

The axial force component of the baseline configuration, Figure 3(a), shows an 8-peak sinusoidal response around the azimuth for both fore and aft rotors. This results from the simultaneous blade passing events owing to equal blade count ($N_1 = N_2 = 4$) and rotational speeds of the baseline configuration. A similar observation can be made for the increased spacing configurations (Figure 3(d)). For the non-axial configuration, Figure 3(b), the axial force shows a single-peaked sinusoidal response characteristic of rotors in non-axial flight which results from the additional velocity component aligned with the rotor rotation, in this case, the downgoing blade. The non-axial case also shows an 8-peak response, resulting from the blade row interaction, overlapped within the single-peaked sinusoidal response. Note that peak values are shown in the same location for fore and aft rotors as the azimuth angle is measured in the relative direction of rotation for each rotor. In reality, the peaks are located on opposing sides of the disc for fore and aft rotors. Further, the negative axial force component for all configurations results from the axes system and does in fact result in positive thrust contributions.

Despite the equal blade count of fore and aft rotors, the axial force of the asynchronous configuration does not show an 8-peak response. Unlike the other configurations, due to unequal rotational speeds of fore and aft rotors, the resulting signal is not periodic within a single rotation. The importance of accounting for the non-periodicity of the signal has previously been highlighted [52, 53]. However, for unequal rotational speeds, a periodic response can only be achieved after a large number of rotations of either fore and aft rotors and this is prohibitively expensive. Therefore, to appropriately capture the non-periodicity, the Vaníček approximation [54, 55] has been applied to the asynchronous configuration data.

The lateral force component (y-direction) of the baseline configuration shows a single-peak sinusoidal response

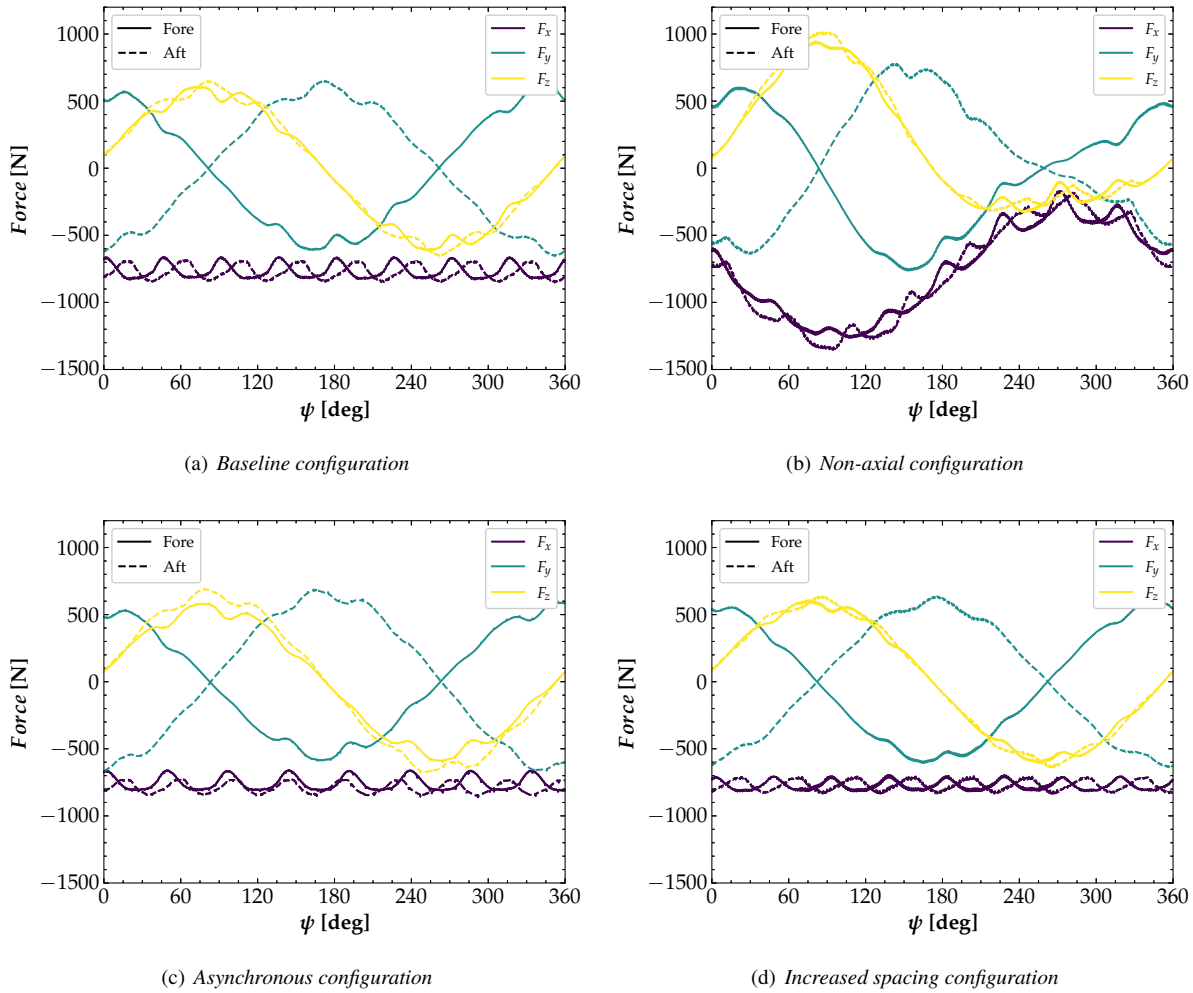

(a) *Baseline configuration*

(b) *Non-axial configuration*

(c) *Asynchronous configuration*

(d) *Increased spacing configuration*

Fig. 3 *Axial force for each configuration.*

around the azimuth. The maximum and minimum values for the fore blade are found where the force component is aligned with the y-axis, i.e. $\psi = 0°$ and $\psi = 180°$ respectively. A similar response is found for the aft blade, only shifted by $\psi = 180°$ resulting from the opposing direction of rotation. The vertical force component shows a very similar response to that of the lateral component. However, for this component, the fore and aft rotors are in-phase, with peak values located where the force vector aligns with the z-direction, $\psi = 90°$. Note again, in reality these would occur on opposite sides of each rotor disc.

Similar behaviour for the lateral and vertical force components are observed for the asynchronous and increased spacing configurations. The small oscillations found within the single period sinusoid illustrates the effects of the blade row interaction on the lateral and vertical force components.

Whilst the non-axial configuration generally shows a similar response to the baseline, the vertical force component shows an increase in the peak force value. Similarly, there is an increase in the minimum value observed. These changes in the force relate to the increased velocity component and subsequent loading in the downgoing blade and the reduced velocity component and subsequent loading in the upgoing blade. The non-zero incidence angle is also shown to affect

the phase of the sinusoidal response. Similarly, the lateral force shows a phase shift relative to the baseline configuration.

To analyse the unsteady loading further, the periodic loadings of the axial component have been transformed to the frequency domain. This affords us the opportunity to study the amplitude of the unsteady loads more closely. The loading on the opposing rotor occurs at frequencies corresponding to [56]:

$$\omega_k = kN_j \left(\frac{\Omega_j}{\Omega_i} + 1 \right) \tag{6}$$

Where, k is the scattering index (0,1,...∞); N is the blade count; and Ω is the rotational speed. i represents the current rotor, whilst j is the opposing rotor. Figure 4 presents the unsteady loading of fore and aft rows in terms of the scattering index, k.

Figure 4 shows that for both fore and aft rotors, the highest amplitudes occur for the even indices, corresponding to twice the blade passage frequency of the opposing rotor. Further, the amplitude of the harmonic loading decreases rapidly for increasing indices. The baseline configuration is generally observed to have the highest amplitudes of unsteady loading of all configurations. The fore rotor of the baseline configuration is shown to have a similar magnitude to the aft rotor for the 2^{nd} index. For subsequent indices, the amplitudes of the fore rotor are generally greater than those of the aft rotor. This highlights the significance of the upstream interactions and agrees with previous findings on the importance of the potential interactions for low-solidity design CROR [6, 7, 20, 57].

The non-axial configuration generally shows the second highest amplitudes of all configurations. Despite the reduced amplitudes of unsteady loading in the axial direction relative to the baseline configuration, the non-axial configuration also has significant amplitudes in the y- and z- directions. The unsteady loading in the y- and z-directions results from the inclination of the disc, resulting in additional velocity components around the disc and subsequently non-axisymmetric loading around the disc. These additional unsteady loads will result in additional contributions to the unsteady loading noise source for this configuration.

The asynchronous configuration shows a significant reduction in amplitude relative to the baseline configuration, owing to the negation of the simultaneous blade passage events which occur for the baseline case. It can also be observed for the asynchronous case that the unsteady loads on the fore rotor tend to be greater than those of the aft rotor. The increased loading on the aft rotor results in an increased potential field and hence the increased unsteady loads on the fore rotor. Whilst reductions in the amplitudes of the axial component were observed for the asynchronous configuration, increased amplitudes of the lateral and longitudinal components were found relative to the baseline configuration.

Finally, turning to the configuration with increased spacing, the amplitudes of unsteady loads of fore and aft rotors are reduced relative to the baseline configuration. Despite the simultaneous blade passage events that also occur for this configuration, the reduction in unsteady loads results from the greater decay of wake and potential fields with the increased distance between fore and aft rotors.

Tip Vortex Interaction (TVI) is unique to CROR configurations and often contributes significantly to the resulting unsteady acoustic emissions. TVI results from the interaction of the aft rotor with the tip vortex system emanating from the fore rotor. In order to examine this interaction, Figure 5 shows a snapshot of the computed flow-field for each configuration. Iso-surfaces of Q-criterion [58] are used to visualise the tip-vortex structures.

Figure 5(a) clearly depicts the interaction of the fore tip vortex with the aft blade row for the baseline configuration. This interaction results in a pressure pulse on the blade surface of the aft blade and consequently contributes to the noise

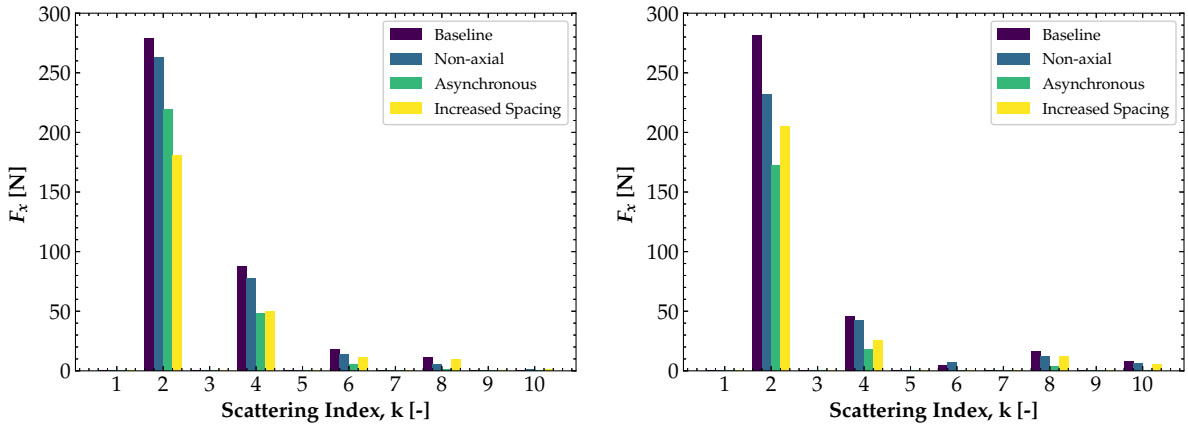

(a) *Fore rotors* (b) *Aft rotors*

Fig. 4 *Harmonic loading on fore and aft rotors for all CROR configurations.*

emission of the CROR. The tip vortex from the aft row is also shown, which subsequently interacts with the tip vortex from the fore row. The contribution of this vortex-vortex interaction to the acoustic emission is not known and cannot be evaluated under the present methodology.

The tip vortices for the non-axial configuration, Figure 5(b), will be skewed in the vertical direction (positive z). Therefore, the interaction with the rear row will not be symmetric around the disc. For blades passing in the positive z-direction, the interaction will be more outboard. Conversely, for those passing in the negative z-direction, the interaction will be more inboard. Therefore, in the study of noise reduction methods for TVI, the off-design cases must also be evaluated as clipping may not be sufficient to suppress the TVI source for some non-axial manoeuvres.

The higher rotation rate of the fore rotor of the asynchronous configuration reduces the loading on the blade row. This reduced loading reduces the strength of the tip vortices and as can be observed in Figure 5(c), the contraction of the tip vortices is not as great as the baseline configuration. Therefore, it would be expected that the TVI source would be greatly reduced for this configuration relative to the baseline case. However, using the present preliminary method where the radial discretisation is used to isolate the sources, the high loading on the outboard portion of the aft blade will still result in contributions to the total noise. Nonetheless, the tip vortex analysis allows us to account for this reduction in TVI.

As the tip vortices (and the viscous) wake propagate downstream, it contracts inwards. Therefore, with an increasing distance between the fore and aft rotors, the tip vortex from the fore rotor will interact with a more inboard section of the aft blade row. This can be observed for the increased spacing configuration, Figure 5(d). The more inboard interaction is expected to result in a greater TVI source as the tip vortex interacts with a greater blade area, particularly for this case where the chord is reduced near the tip.

V. Aeroacoustic Analysis

Aeroacoustic simulations were carried out to evaluate the noise emissions for all configurations. The HMB solver was coupled to the Farassat 1A code to compute the far-field tonal noise based on blade surface pressure data.

The noise of each configuration was evaluated at a simulated constant-altitude flyover, with $h = 304.8$m. The flyover

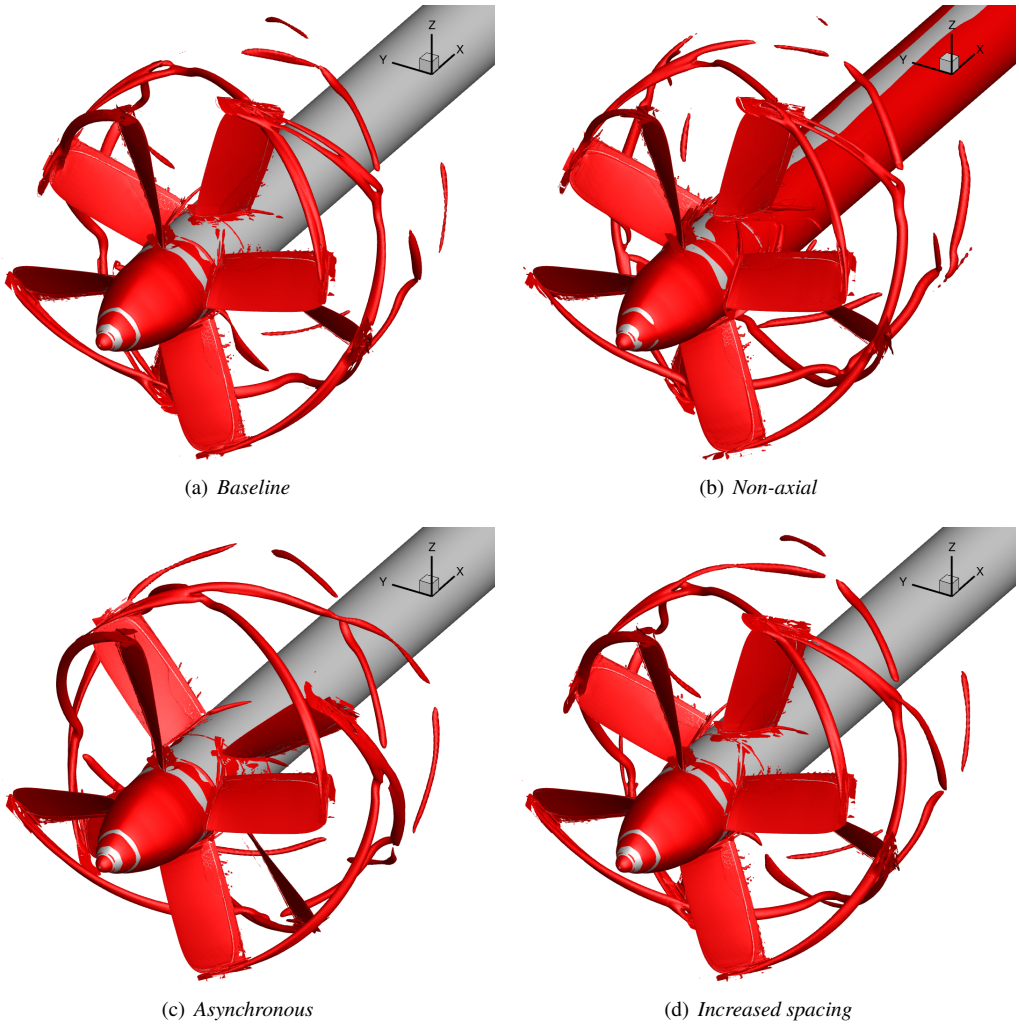

(a) *Baseline* (b) *Non-axial*

(c) *Asynchronous* (d) *Increased spacing*

Fig. 5 *Iso-surfaces of Q-criterion to visualise tip vortices, Q=0.2 for all cases.*

was simulated by an array of numerical microphones placed directly below the CROR along the axis of rotation. The numerical microphones were positioned between the two polar angle extremes with a separation corresponding to 0.5s to allow for accurate computation of the EPNL over the simulated flyover. The polar angle is defined according to Figure 6 which also shows the positioning of the numerical microphone array for the flyover.

Figure 7 presents the polar directivities computed for all configurations, where the reported SPL values have been calculated directly from the time pressure signals computed from the acoustic code. In addition to the highest peak levels, the non-axial configuration is observed to produce the highest SPL levels across all polar angles. The baseline configuration shows the second-highest peak levels, followed by the asynchronous configuration. Whilst the baseline configuration shows a higher level in the aft-ward arc, the asynchronous configuration shows a greater level in the fore arc. Showing the lowest levels over all polar angles is the increased spacing configuration, demonstrating significant reductions in computed SPL relative to all other configurations.

The EPNL and LA_{max} are common metrics in aircraft certification that are used to characterise the noise in terms of a single value accounting for a range of acoustic effects. Table 3 presents the computed EPNL and LA_{max} for all

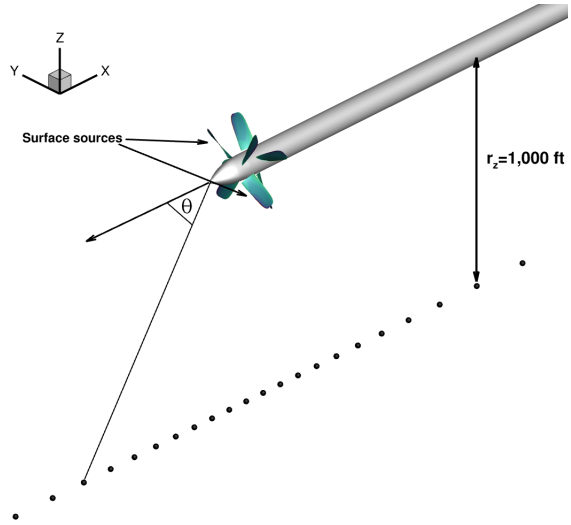

Fig. 6 *Microphone locations for aeroacoustic analysis* (*note*: *positions not to scale and not every point shown*).

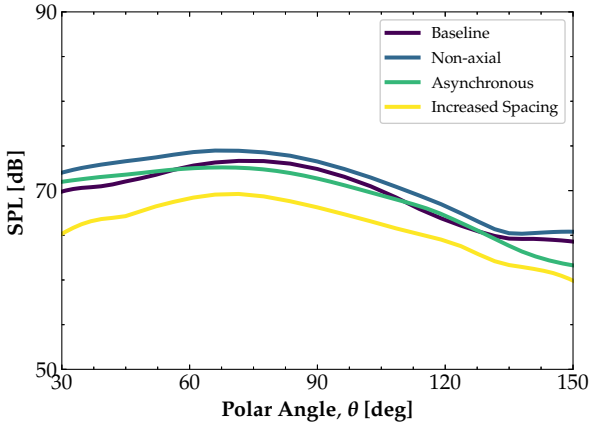

Fig. 7 *Computed polar directivities for each configuration.*

configurations. The non-axial configuration is again shown to have the highest noise levels in terms of both metrics. This is followed by the baseline configuration. Using the EPNL metric, the asynchronous configuration is only slightly reduced relative to the baseline configuration. On the other hand, using the LA_{max} metric, there is a more clear difference and reduction in noise level from the asynchronous configuration. Again, the increased spacing configuration shows the lowest levels in terms of both metrics. Note, however, there is a small difference in terms of LA_{max} between the increased spacing and asynchronous configurations.

In order to investigate the differences between the configurations, we will attempt to dissect the total noise levels to identify the contributions of the various noise sources. In doing so, the noise dissection should better explain the observed differences between configurations and help to identify noise reduction strategies for future CROR designs for general aviation class aircraft.

Figures 8-11 show the polar directivity for the CROR noise sources for all configurations. All configurations show a number of similar trends over the directivity. Firstly, all configurations are shown to have high SPL levels at the polar

Table 3 *Computed noise levels for each configuration.*

Configuration	EPNL [dB]	$LA_{\max}$ [dBA]
Baseline	75.79	67.51
Non-axial	77.91	68.78
Asynchronous	75.27	65.84
Increased Spacing	72.75	65.23

angle extremes. These high levels are a result of the unsteady loading on each blade row. Contrary to the sharp drop away from the overhead position typically shown for isolated rotors, these high levels show the importance of reducing the unsteady source for CROR. Also common among all configurations is the behaviour of the contributions from fore and aft rows. Whilst the fore sources shows a peak level in the forward arc, the aft sources show a peak in the aft-ward arc. Finally, for all configurations, the peak level lies in the forward arc. This may initially result from the effect of the Doppler shift moving the sources from the overhead position. However, comparing fore and aft sources for each configuration shows that the fore rotor has a greater peak noise level, suggesting the fore rotor, and the upstream unsteady interactions, to be the most significant source for the present configurations.

Investigating each configuration more closely and beginning with the baseline configuration, Figure 8 presents the contribution from each noise source for both fore and aft rotors over the polar directivity. The fore sources are dominated in the up and downstream directions by the unsteady noise sources. However, near the rotor plane, the steady loading sources are shown to make a significant contribution to the overall SPL. The thickness source is found to not contribute significantly over the entire polar angle range and in fact, is the case for all configurations due to the equal design of the blade rows. However, as tip speed and forward speed increase, e.g. as the aircraft enters cruise, the thickness source will become more important.

Turning to the aft rotor sources of the baseline configuration, a similar trend is observed to the fore configuration, with high levels at the extreme polar angles due to the unsteady loading sources. Further similarities are observed near the rotor plane with high steady loading contributions. The unsteady loadings sources are further grouped as wake and potential and TVI sources. The TVI shows a similar trend, although a reduced level, to the wake and potential sources over the range of polar directivity angles. However, the peak level of the TVI source at $\sim \theta = 125°$ shows an almost equal level to the wake and potential sources. The high levels demonstrate the importance of clipping the aft rotor to reduce the TVI source.

The source contributions for the non-axial configuration are presented in Figure 9 . Concerning the fore rotor sources, over the entire directivity, the total noise is dominated by the unsteady sources. The same behaviour is also observed for the aft rotor sources. The non-zero angle of the blade rows for the non-axial configuration results in additional velocity components and subsequently non-axisymmetric loading over the disc. Therefore, despite the reduction in unsteady axial loading (Figure 4), the non-axial configuration has significant unsteady loads in the y- and z- directions. These additional unsteady loading components result in an increased unsteady noise source for both rotors of the non-axial configuration.

Due to the non-zero incidence angle of the disc, the interaction of the tip vortex with the rear row occurs at different span-wise locations around the disc. Whilst for the blades in the lower disc area the interaction moves more inboard, those in the upper area are much less affected as the tip vortex moves away from the rear rotor blade. Consequently,

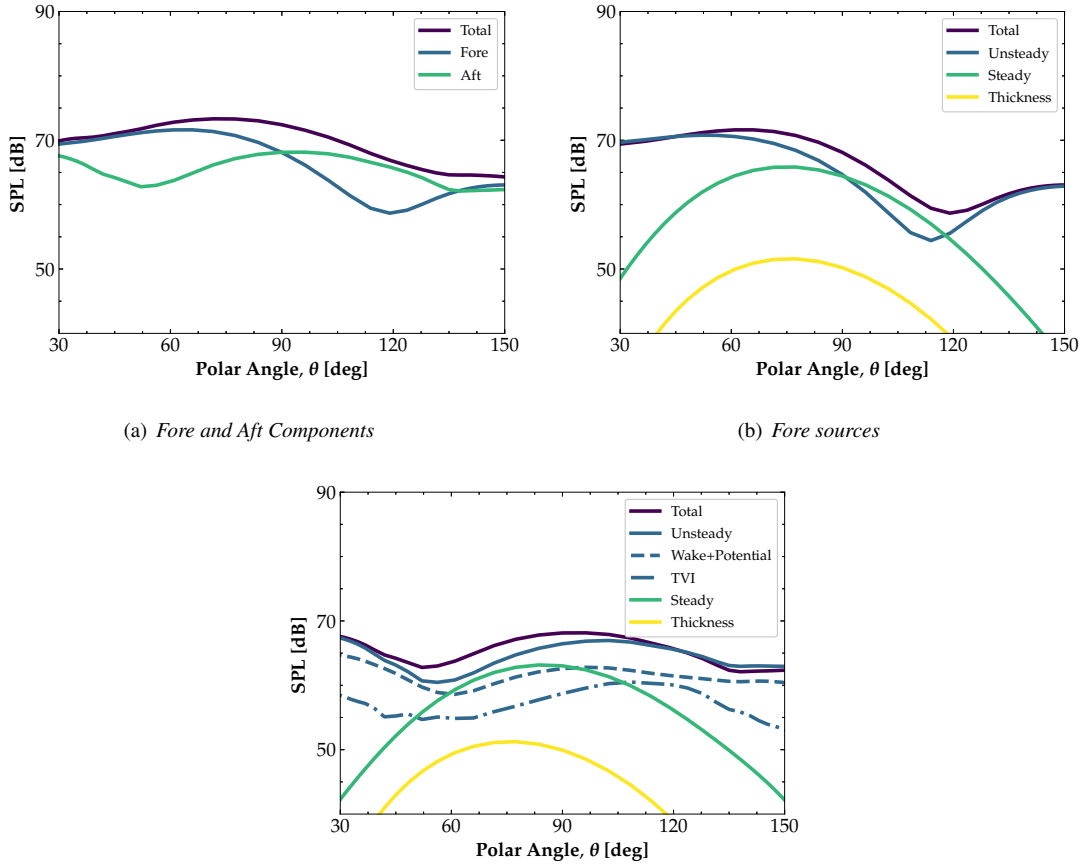

(a) *Fore and Aft Components*

(b) *Fore sources*

(c) *Aft sources*

Fig. 8 *Noise source components for baseline configuration.*

the aft sources are dominated by the wake and potential effects, where the TVI source makes a much lower relative contribution to the total unsteady source.

Compared with the directivity trends of the fore rotor of the baseline configuration, the non-axial configuration shows a increased level of peak SPL. Similarly, the aft rotor shows a greater SPL over the most directivities. Comparing the dissected sources, it is apparent that the increased SPL levels observed for the non-axial case over the polar angle range is due to the increased unsteady loading (combined across all axes) relative to the baseline configuration. Furthermore, whilst there are some areas where either fore or aft rotor of the non-axial configuration is less than the baseline configuration, their combined contribution results in a greater total noise level over the baseline case over the directivity range.

The asynchronous configuration source directivities are presented in Figure 10. The fore sources are dominated at the extreme polar angles by the unsteady sources, with the steady component proving more significant near the rotor plane. A similar observation can be made for the aft sources. Note that the fore rotor shows an increase in thickness source, whilst the aft shows a reduction, resulting from the change in rotational speed from the baseline.

The wake and potential sources dominate the aft unsteady sources over most directivities, with the exception where the peak level of the TVI source at $\sim \theta = 125°$ shows an equal value to the wake and potential source. However, there

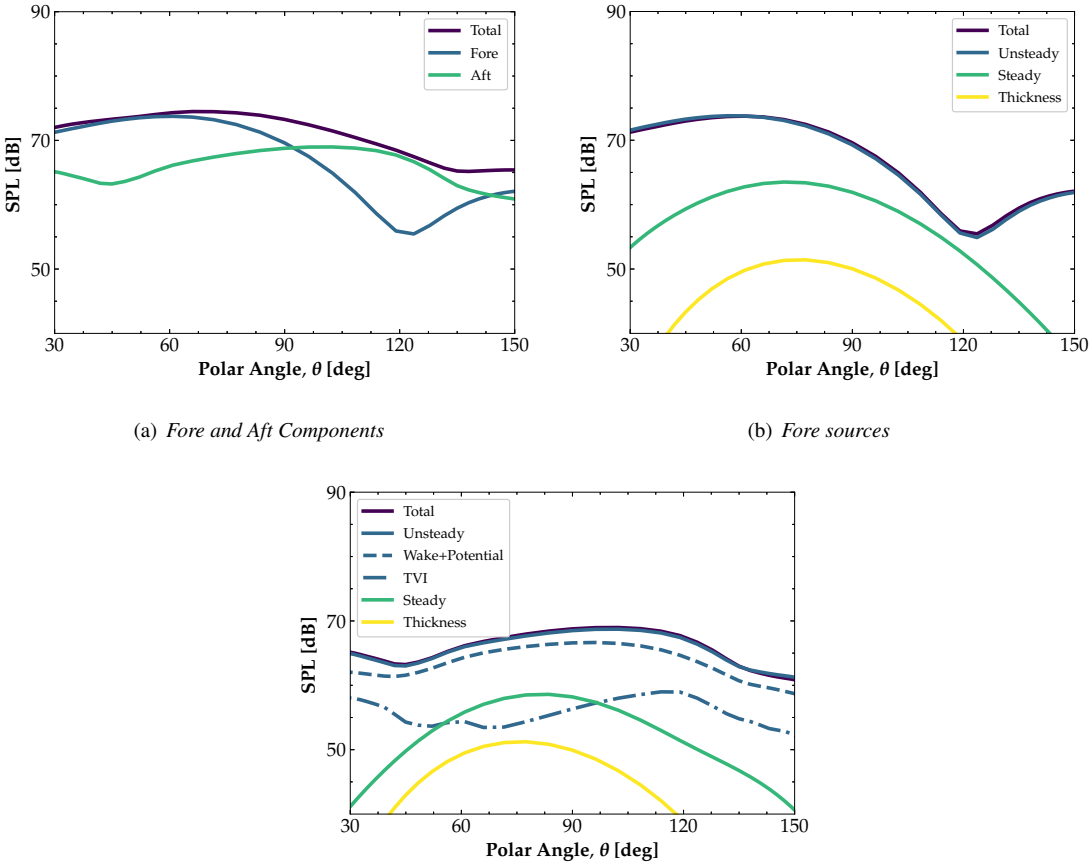

(a) *Fore and Aft Components*

(b) *Fore sources*

(c) *Aft sources*

Fig. 9 *Noise source components for non-axial configuration.*

must be some caution in using this result. Figure 5 showed that the interaction of the tip vortex for the asynchronous configuration was much more outboard than the baseline configuration. Whilst the TVI source does show a reduction from the baseline configuration, the presented sources are likely much more heavily controlled by the wake and potential effects in the outermost 15% of the blade (i.e. the cut-off for the TVI source).

Comparing the fore sources with the baseline configuration, the directivity trends are relatively comparable up until the overhead position. After this, the baseline configuration decreases more rapidly up until around $\theta = 120°$ where the baseline configuration increases above the level of the asynchronous configuration. The regions of increased SPL for the asynchronous configuration relate back to an increase in the unsteady source. Whilst inspection of the axial unsteady loading showed reduced levels relative to the baseline, the asynchronous configuration demonstrated higher unsteady loading in the lateral and longitudinal directions which are hypothesized to be responsible for the region of increased SPL in the unsteady noise source for the fore rotor.

Comparing the aft rotor sources, the asynchronous configuration generally shows reduced levels relative to the baseline configuration over the range of polar directivity angles. Looking at the source components, this results from a reduction of the unsteady source and can be traced back to a significant drop the unsteady loading. However, with the fore rotor being the dominant source, the total directivity trend, Figure 7, is comparable to the fore rotor trend and

subsequently the baseline configuration.

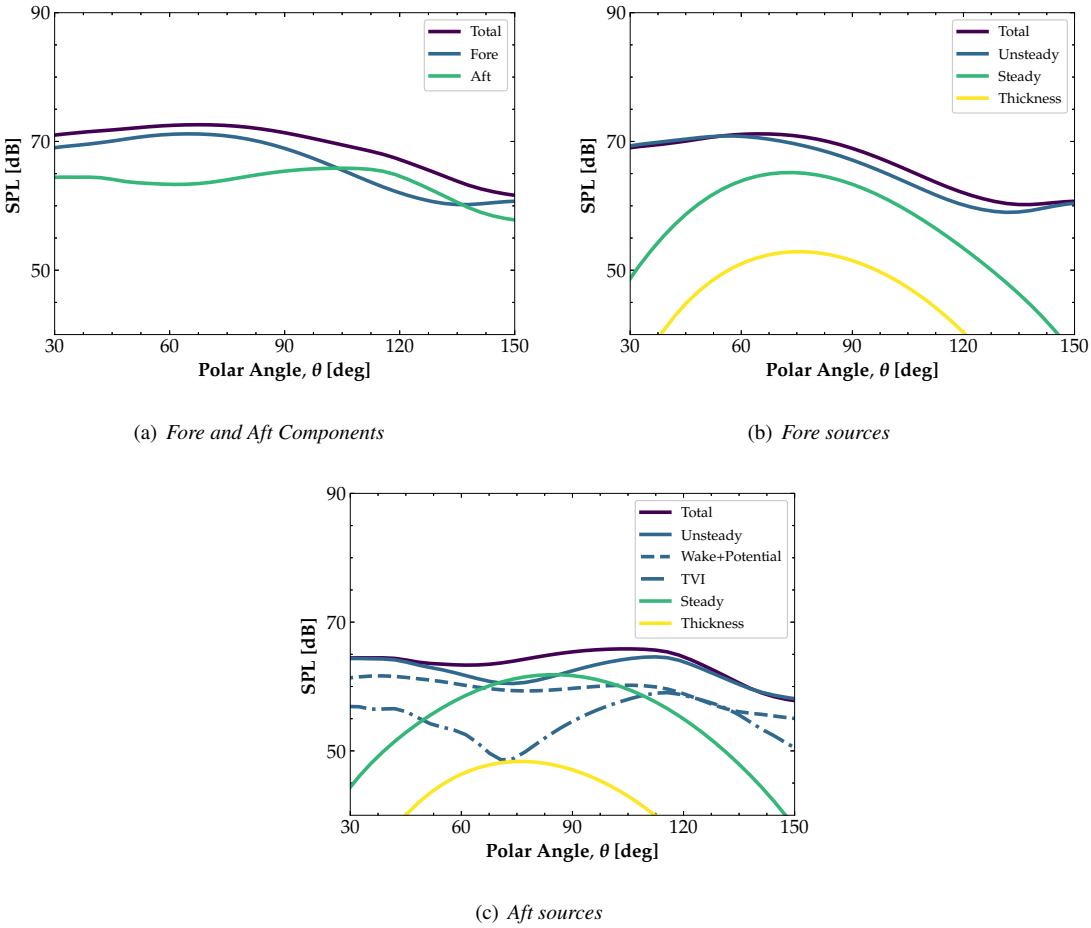

(a) *Fore and Aft Components*

(b) *Fore sources*

(c) *Aft sources*

Fig. 10 *Noise source components for asynchronous configuration.*

The computed source directivities for the increased spacing configuration are shown in Figure 1 1. The fore rotor shows the dominance of the unsteady component at the extreme polar angles, with the steady component making a significant contribution to the total noise near the rotor p lane. A similar observation is made for the aft r otor. Looking closer at the aft rotor unsteady components, the TVI source is shown to make a relatively more significant contribution to the unsteady source when compared to the baseline configuration. The increase in the relative contribution of the TVI source relates to the increase in spacing and the subsequent inboard movement of the interaction of the aft rotor with the fore rotor tip vortex.

Comparing the fore directivity trends with those of the baseline configuration, the increased spacing configuration shows the lowest SPL values over most directivity angles. The significant reductions observed for this configuration relate back to the substantial reduction in unsteady loading that has been demonstrated which itself results from the increased spacing and the subsequent decay of the potential field.

Regarding the aft rotor, the increased spacing configuration has reduced values of SPL relative to the baseline configuration. However, the levels are comparable to the asynchronous c onfiguration. Nonetheless, the fore rotor remains the dominant source and as a result the total noise of the increased spacing configuration remains the lowest over

the entire polar directivity range, owing to the reduction in unsteady periodic loading that results from the rotor-rotor interaction.

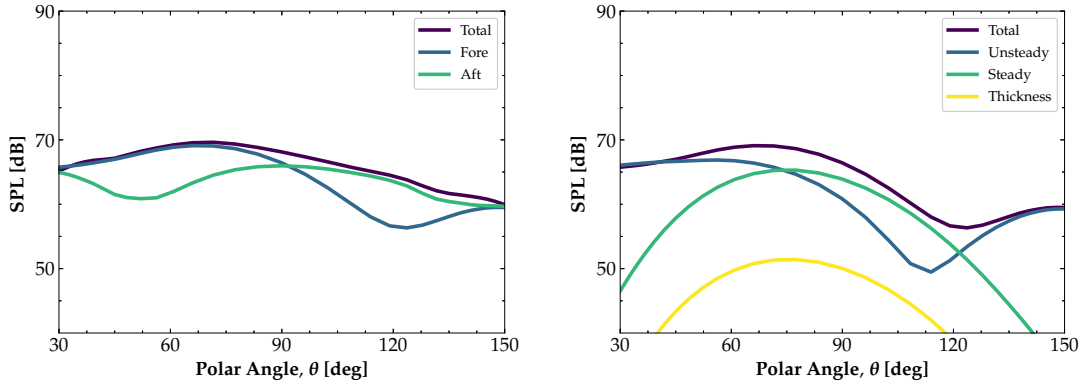

(a) *Fore and Aft Components* (b) *Fore sources*

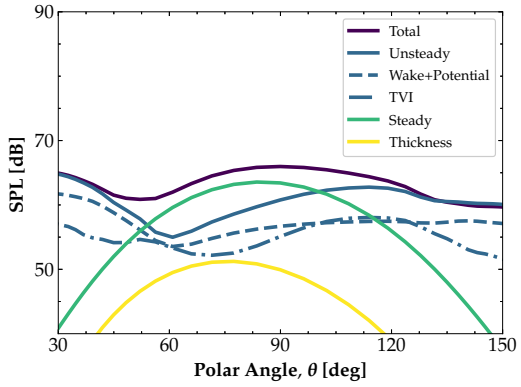

(c) *Aft sources*

Fig. 11 *Noise source components for increased spacing configuration.*

From the discretisation of the noise sources for each configuration, their relative contribution to the total EPNL could be computed. Figure 12 presents the contribution of sources to the computed EPNL for each configuration. Comparing the contributions of fore and aft rotors Figure 12(a) shows that for all configurations, the fore rotor is the dominant source. This confirms the dominance of the fore rotor found in the analysis of the polar directivities of each configuration. Furthermore, this is also reflected in the analysis of the unsteady loading which suggested the loading on the fore rotor to be greater than that of the aft and also further highlights the importance of the potential field interactions for the present case of low-solidity rotor designs.

Looking at the contributions for fore and aft rotors for all configurations, the unsteady source is the dominant contributor to the total EPNL. Therefore, efforts at reducing CROR noise should be directed towards this component in order to make significant gains in terms of noise reduction. Nonetheless, the steady noise still contributes significantly to the overall noise, and in particular near the overhead position as was also demonstrated in the analysis of the polar directivities. Subsequently, steady noise sources should also be targeted in the reduction of the CROR noise. The steady source shows variation between configurations and was found to be a result of differences in the steady loading. With

the exception of the asynchronous configuration, the thickness source should be equal for all other configurations due to the equal design and rotational speed of the blade rows. Further analysis of the configurations showed a much quicker decay of harmonics for the non-axial and increased spacing configuration, resulting in much lower EPNL values for the steady components.

Turning to the aft blade rows, Figure 12(c), the TVI source can be seen to play an important part in the total noise emission for each configuration. In fact, for the increased spacing configuration, the TVI source is found to be greater than that of the wake and potential sources. This was related to the higher frequency components of the TVI source. However, the results for the TVI source must be used with caution. The preliminary methodology discretised the aft sources based on blade location. Therefore, in addition to the effects of the tip vortex, the TVI sources will also contain the wake and potential sources for the outboard portion of the blade. Nonetheless, the preliminary method can provide a suitable indication of the relative contribution so long as it is supported by an aerodynamic analysis.

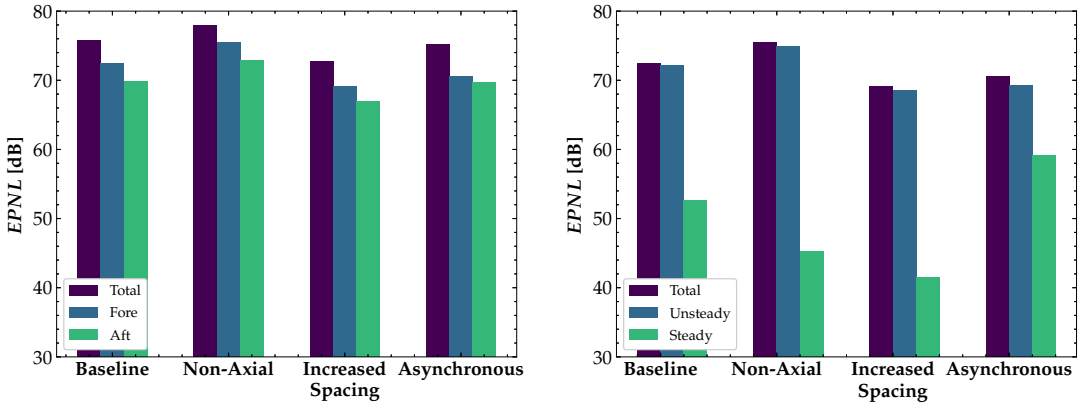

(a) *Total, fore and aft Components*

(b) *Fore sources*

(c) *Aft sources*

Fig. 12 *EPNL source breakdown for each configuration.*

The analysis of all configurations has shown that tonal noise reductions can be achieved through non-equal rotational speeds of fore and aft rotors and increasing the rotor-rotor spacing. The asynchronous configuration removes the simultaneous blade passage of fore and aft rotors, reducing the unsteady loading and subsequent noise emissions. Furthermore, off-loading the fore rotor reduced the unsteady interactions on the aft rotor. In the present case where

the fore sources dominate, it may have been more beneficial to increase the aft rotational speed in order to reduce the magnitude of the unsteady loading on the fore rotor. Whilst the change of rotational speed was found to reduce the propulsive efficiency, optimisation of the rotational speeds may find suitable reductions in noise for more favourable aerodynamic performance. A similar result may be achieved through changes in blade count and should also be considered within the CROR design. In the case of increased spacing, noise reductions are achieved due to the decay of wake and potential fields. However, increasing the spacing does result in an increase in wake contraction, and in the case where clipping is used, it becomes less effective at reducing the TVI source. Nonetheless, previous methods to reduce interaction noise are focused on minimising the wake interaction source. In the present case where the upstream potential interactions are more significant, increased spacing appears more favourable due to the rapid decay of the potential field. Further increasing the spacing between the rotors would result in reduction in the noise, primarily driven by a reduction in the interaction between the two blade rows. However, further increased spacing would eventually result in reductions in efficiency of the CROR as the two rotors cannot benefit from their interaction (i.e., conversion of angular momentum to useful thrust). The non-axial configuration showed the greatest noise levels due to the further unsteady loading introduced through operation at non-axial conditions. The analysis demonstrated the need to evaluate noise-reducing strategies at off-design conditions, particularly at take-off, where noise evaluation is perhaps the most important.

VI. Conclusions

An aerodynamic and aeroacoustic evaluation of a number of isolated CROR configurations has been carried out. Alongside the baseline configuration, a CROR at a non-zero incidence angle, a CROR with non-equal fore and aft rotational speeds and a CROR with increased rotor-rotor spacing has been studied. All configurations had an equal fore and aft blade count. Furthermore, for each configuration operational and geometric parameters were kept constant with the exception of the parameter of interest. Due to the inherent complexities of CROR noise, the present study has undertaken to use a preliminary methodology to isolate the individual sources. Whilst our work is limited to the tonal sources (broadband and quadrupole sources have been neglected), it remains useful in identifying CROR noise sources and will be used to better direct future work in CROR noise reduction for general aviation aircraft.

For all configurations the noise from the fore rotor was found to be the dominant source, highlighting the importance of the upstream potential interactions for the present case of low-solidity rotors. Subsequently, noise reductions were observed for the increased spacing configuration where there was a significant reduction in the unsteady loads as a result of the decay of potential field and viscous wake.

The baseline configuration demonstrates sub-optimal acoustic performance due to the simultaneous blade passage that occurs due to the equal fore and aft blade counts and rotation rates. Noise reductions were observed when fore and aft rotor rotational speeds were not equal, resulting from a reduction in the unsteady loading. Although, this was accompanied by a reduction in aerodynamic performance. However, optimisation of the fore and aft rotational speed is likely to deliver reductions in noise without severely impacting aerodynamic performance.

Every CROR will face operation in non-axial inflow, with take-off perhaps being the most pertinent for acoustic evaluation. Analysis of the CROR with non-axial inflow demonstrated increased noise levels relative to the baseline. This highlights the need to evaluate noise-reducing strategies at off-design cases to really prove their noise reduction capabilities.

The present study was carried out to investigate the noise sources of various CROR configurations in order to steer future CROR designs with reduced noise levels. An aerodynamic and acoustic analysis showed that increased spacing and asynchronous rotational speeds could be employed subject to further consideration of tip vortex interaction and aerodynamic performance. The present study demonstrated the ability to reduce various CROR noise sources and where further work should be directed. However, it also showed the need to consider the aerodynamic trade-offs. Future work should take a combined approach where both aerodynamic and aeroacoustic performance are simultaneously optimised in order to retain the high propulsive efficiency at cruise the CROR is famed for. Additionally, future work on noise-reducing strategies should also be scrutinised at off-design cases, in particular at take-off, due to the importance of low noise in this phase of flight.

Funding Sources

This research is supported by a private sponsorship (Mr Mike Newton) and a UK Research Council Grant EP/S010092/1 (Methods and Experiments for Novel Rotorcraft).

Acknowledgments

The authors would like to acknowledge the use of the Cirrus UK National Tier-2 HPC Service at EPCC (http://www.cirrus.ac.uk) funded by the University of Edinburgh and EPSRC (EP/P020267/1). The authors would also like to acknowledge the assistance given by Research IT, and the use of The HPC Pool funded by the Research Life cycle Programme at The University of Manchester. This work also benefitted from the aeroacoustics research within the UK Acoustics Network, EPSRC Grant EP/V007866/1

References

[1] Van Zante, D. E., "Progress in Open Rotor Research: A U.S. Perspective," *ASME Turbo Expo 2015*, Montréal, Canada, 2015, pp. 1–14. https://doi.org/10.1115/GT2015-42203.

[2] Delattre, G., and Falissard, F., "Influence of Torque Ratio on Counter-Rotating Open-Rotor Interaction Noise," *AIAA Journal*, Vol. 53, No. 9, 2015, pp. 2726–2738. https://doi.org/10.2514/1.J053797.

[3] Stuermer, A., and Yin, J., "Low-Speed Aerodynamics and Aeroacoustics of CROR Propulsion Systems," *15th AIAA/CEAS Aeroacoustics Conference (30th AIAA Aeroacoustics Conference)*, 2009. https://doi.org/10.2514/6.2009-3134.

[4] Magliozzi, B., Hanson, D. B., and Amiet, R. K., "Propeller and Propfan Noise," *NASA Langley Research Center, Aeroacoustics of Flight Vehicles: Theory and Practice. Volume 1: Noise Sources*, 1991.

[5] Hanson, D. B., and Fink, M. R., "The importance of quadrupole sources in prediction of transonic tip speed propeller noise," *Journal of Sound and Vibration*, Vol. 62, No. 1, 1979, pp. 19–38. https://doi.org/10.1016/0022-460X(79)90554-6.

[6] Bradley, A. J., "A study of the rotor/rotor interaction tones from a contra-rotating propeller driven aircraft," *AIAA 10th Aeroacoustics Conference*, Seattle, Washington, 1986. https://doi.org/10.2514/6.1986-1894.

[7] Parry, A. B., and Crighton, D. G., "Asymptotic theory of propeller noise. I - Subsonic single-rotation propeller," *AIAA Journal*, Vol. 27, No. 9, 1989, pp. 1184–1190. https://doi.org/10.2514/3.10244.

[8] Smith, D. A., Filippone, A., and Barakos, G. N., "Acoustic Analysis of Counter-Rotating Open Rotors with a Locked Blade Row," *AIAA Journal*, Vol. 58, No. 10, 2020. https://doi.org/10.2514/1.J059273.

[9] Gentry Jr., G. L., Booth Jr., E. R., and Takallu, M. A., "Effect of Pylon Wake With and Without Pylon Blowing on Propeller Thrust," *NASA TM 4162*, 1990.

[10] Kleinert, J., Dürrwächter, L., Keßler, M., and Krämer, E., "Aeroacoustics of High-Fidelity URANS Simulations of a Model Contra-Rotating Open Rotor with Mounting Pylon," *2018 AIAA/CEAS Aeroacoustics Conference*, 2018. https://doi.org/10.2514/6.2018-4082.

[11] Sohoni, N. G., Hall, C. A., and Parry, A. B., "The influence of an upstream pylon on open rotor aerodynamics at angle of attack," *Journal of Turbomachinery*, Vol. 141(2), No. 021006, 2018. https://doi.org/10.1115/1.4041082.

[12] Brandvik, T., Hall, C., and Parry, A. B., "Angle-of-Attack Effects on Counter-Rotating Propellers at Take-Off," *Proceedings of the ASME Turbo Expo 2012: Turbine Technical Conference and Exposition. Volume 8: Turbomachinery, Parts A, B, and C.*, 2012, pp. 523–534. https://doi.org/10.1115/GT2012-69901.

[13] Parry, A. B., Kingan, M., and Tester, B. J., "Relative importance of open rotor tone and broadband noise sources," *17th AIAA/CEAS Aeroacoustics Conferencez (32nd AIAA Aeroacoustics Conference)*, 2011. https://doi.org/10.2514/6.2011-2763.

[14] Kingan, M. J., "Open Rotor Broadband Interaction Noise," *Journal of Sound and Vibration*, Vol. 332, No. 17, 2013, pp. 3956–3970. https://doi.org/10.1016/j.jsv.2013.03.014.

[15] Hanson, D. B., "Influence of Propeller Design Parameters on Far-Field Harmonic Noise in Forward Flight," *AIAA Journal*, Vol. 18, No. 11, 1980, pp. 1313–1319. https://doi.org/10.2514/3.50887.

[16] Hanson, D. B., "Noise of Counter-Rotation Propellers with Non-Synchronous Rotors," *Journal of Aircraft*, Vol. 22, No. 12, 1985, pp. 1097–1099. https://doi.org/10.2514/3.45173.

[17] Dittmar, J. H., "Some Design Philosophy for Reducing the Community Noise of Advanced Counter- Rotation Propellers," *NASA TM 87099*, 1985.

[18] Parry, A. B., and Vianello, S., "A project study of open rotor noise," *International Journal of Aeroacoustics*, Vol. 11, No. 2, 2012, pp. 247–258. https://doi.org/10.1260/1475-472X.11.2.247.

[19] Smith, D. A., Filippone, A., and Bojdo, N., "A Parametric Study of Counter Rotating Open Rotor Noise," *25th AIAA/CEAS Aeroacoustics Conference*, Delft, The Netherlands, 2019. https://doi.org/10.2514/6.2019-2570.

[20] Smith, D. A., Filippone, A., and Bojdo, N., "Noise reduction of a Counter Rotating Open Rotor through a locked blade row," *Aerospace Science and Technology*, Vol. 98, No. 105637, 2020. https://doi.org/10.1016/j.ast.2019.105637.

[21] Woodward, R. P., "Noise of a Model High Speed Counterrotation Propeller at Simulated Takeoff/Approach Conditions (F7/A7)," *NASA TM 100206*, 1987.

[22] Schnell, R., Yin, J., Voss, C., and Nicke, E., "Assessment and Optimization of the Aerodynamic and Acoustic Characteristics of a Counter Rotating Open Rotor," *Journal of Turbomachinery*, Vol. 134, No. 6, 2012. https://doi.org/10.1115/1.4006285.

[23] Roger, M., Schram, C., and Moreau, S., "On vortex-airfoil interaction noise including span-end effects, with application to open-rotor aeroacoustics," *Journal of Sound and Vibration*, Vol. 333, No. 1, 2014, pp. 283–306. https://doi.org/10.1016/j.jsv.2013.09.012.

[24] Woodward, R. P., and Gordon, E. B., "Noise of a Model Counterrotation Propeller With Reduced Aft Rotor Diameter and Simulated Takeoff/Approach Conditions (F7/A3)." *26th Aerospace Sciences Meeting*, 1988. https://doi.org/10.2514/6.1988-263.

[25] Dittmar, J. H., and Stang, D. B., "Reduction of the noise of a model counterrotation propeller at cruise by reducing the aft propeller diameter," *The Journal of the Acoustical Society of America*, Vol. 81, No. S1, 1987. https://doi.org/10.1121/1.2024493.

[26] Negulescu, C. A., "Airbus AI-PX7 CROR Design Features and Aerodynamics," *SAE International Journal of Aerospace*, Vol. 6, No. 2, 2013, pp. 626–642. https://doi.org/10.4271/2013-01-2245.

[27] Van Zante, D. E., Collier, F., Orton, A., Khalid, S. A., Wojno, J. P., and Wood, T. H., "Progress in open rotor propulsors: The FAA/GE/NASA open rotor test campaign," *Aeronautical Journal*, Vol. 118, No. 1208, 2014, pp. 1181–1213. https://doi.org/10.1017/S0001924000009842.

[28] Peters, A., and Spakovszky, Z. S., "Rotor interaction noise in counter-rotating propfan propulsion systems," *Proceedings of the ASME Turbo Expo*, Vol. 134, 2010. https://doi.org/10.1115/GT2010-22554.

[29] Grasso, G., Moreau, S., Christophe, J., and Schram, C., "Multi-disciplinary optimization of a contra-rotating fan," *International Journal of Aeroacoustics*, Vol. 17, No. 6-8, 2018, pp. 655–686. https://doi.org/10.1177/1475472X18789000.

[30] Lepot, I., Leborgne, M., Schnell, R., Yin, J., Delattre, G., Falissard, F., and Talbotec, J., "Aero-Mechanical Optimization of a Contra-Rotating Open Rotor and Assessment of its Aerodynamic and Acoustic Characteristics," *Proceedings of the Institution of Mechanical Engineers Part A-Journal of Power and Energy*, Vol. 225, No. A7, 2011, pp. 850–863. https://doi.org/10.1177/0957650911413695.

[31] Filippone, A., and Mohamed-Kassim, Z., "Multi-disciplinary simulation of propeller-turboprop aircraft flight," *Aeronautical Journal*, Vol. 116, No. 1184, 2012, pp. 985–1014. https://doi.org/10.1017/S0001924000007454.

[32] Filippone, A., "Aircraft Noise: Noise Sources," *Advanced Aircraft Flight Performance*, Cambridge University Press, 2012, pp. 470–532. https://doi.org/10.1017/CBO9781139161893.

[33] Stuermer, A., "Unsteady CFD Simulations of Contra-Rotating Propeller Propulsion Systems," *44th AIAA/ASME/SAE/ASEE Joint Propulsion Conference & Exhibit*, 2008. https://doi.org/10.2514/6.2008-5218.

[34] Stuermer, A., and Yin, J., "Aerodynamic and Aeroacoustic Analysis of Contra-Rotating Open Rotor Propulsion Systems at Low-Speed Flight Conditions," *Notes on Numerical Fluid Mechanics and Multidisciplinary Design*, Vol. 112, 2010, pp. 481–488. https://doi.org/10.1007/978-3-642-14243-7_59.

[35] Zachariadis, A., Hall, C., and Parry, A. B., "Contrarotating Open Rotor Operation for Improved Aerodynamics and Noise at Takeoff," *Journal of Turbomachinery*, Vol. 135, 2013. https://doi.org/10.1115/1.4006778.

[36] Soulat, L., Kernemp, I., Moreau, S., and Fernando, R., "Numerical assessment of the noise emission of Counter-Rotating Open Rotors," *10th European Conference on Turbomachinery Fluid Dynamics & Thermodynamics*, 2013. https://doi.org/10.1177/1475472X16630861.

[37] Stuermer, A., and Yin, J., "Aerodynamic and Aeroacoustic Installation Effects for Pusher-Configuration CROR Propulsion Systems," *28th AIAA Applied Aerodynamics Conference*, 2010. https://doi.org/10.2514/6.2010-4235.

[38] Delattre, G., Falissard, F., Vion, L., and Jacquin, L., "Open rotor interaction noise reduction through front rotor wake modification," *International Journal of Aeroacoustics*, Vol. 15, No. 1-2, 2016, pp. 207–227. https://doi.org/10.1177/1475472X16643461.

[39] Barakos, G., Steijl, R., Badcock, K., and Brocklehurst, A., "Development of CFD Capability for Full Helicopter Engineering Analysis," *31st European Rotorcraft Forum*, 2005.

[40] Steijl, R., Barakos, G., and Badcock, K., "A Framework for CFD Analysis of Helicopter Rotors in Hover and Forward Flight." *International Journal for Numerical Methods in Fluids*, Vol. 51, No. 8, 2006, pp. 819–847. https://doi.org/10.1002/fld.1086.

[41] Hirt, C., Amsden, A., and Cook, J., "An Arbitrary Lagrangian-Eulerian Computing Method for All Flow Speeds," *Journal of Computational Physics*, Vol. 135, No. 2, 1997, pp. 203–216. https://doi.org/10.1006/jcph.1997.5702.

[42] Menter, F. R., "Two-equation eddy-viscosity turbulence models for engineering applications," *AIAA Journal*, Vol. 32, No. 8, 1994, pp. 1598–1605. https://doi.org/10.2514/3.12149.

[43] Osher, S., and Chakravarthy, S., "Upwind schemes and boundary conditions with applications to Euler equations in general geometries," *Journal of Computational Physics*, Vol. 50, No. 3, 1983, pp. 447–481. https://doi.org/10.1016/0021-9991(83)90106-7.

[44] van Leer, B., "Towards the ultimate conservative difference scheme. V. A second-order sequel to Godunov's method," *Journal of Computational Physics*, Vol. 32, No. 1, 1979, pp. 101–136. https://doi.org/10.1016/0021-9991(79)90145-1.

[45] van Albada, G. D., van Leer, B., and Roberts Jr., W. W., "A Comparative Study of Computational Methods in Cosmic Gas Dynamics," *Astronomy and Astrophysics*, Vol. 108, No. 1, 1982, pp. 76–84. https://doi.org/10.1007/978-3-642-60543-7_6.

[46] Axelsson, O., *Iterative Solution Methods*, Cambridge University Press, 1994. https://doi.org/10.1016/j.apnum.2004.06.003.

[47] Barakos, G. N., and Johnson, C. S., "Acoustic comparison of propellers," *International Journal of Aeroacoustics*, Vol. 15, No. 6-7, 2016, pp. 575–594. https://doi.org/10.1177/1475472X16659214.

[48] Chirico, G., Barakos, G. N., and Bown, N., "Numerical aeroacoustic analysis of propeller designs," *Aeronautical Journal*, Vol. 122, No. 1248, 2018, pp. 283–315. https://doi.org/10.1017/aer.2017.123.

[49] Jimenez-Garcia, A., Barakos, G. N., and Gates, S., "Tiltrotor CFD Part I - Validation," *Aeronautical Journal*, Vol. 121, No. 1239, 2017, pp. 577–610. https://doi.org/10.1017/aer.2017.17.

[50] Smith, D. A., "Aerodynamic and Aeroacoustic Analysis of Counter Rotating Open Rotors," Ph.D. thesis, University of Manchester, 2020.

[51] Farassat, F., "Linear Acoustic Formulas for Calculation of Rotating Blade Noise," *AIAA Journal*, Vol. 19, No. 9, 1981, pp. 1122–1130. https://doi.org/10.2514/3.60051.

[52] Akkermans, R. A., Delfs, J. W., Lummer, M., Siefert, M., Caruelle, B., and Tiedemann, C., "Handling of non-periodic contra rotating open rotor data," *18th AIAA/CEAS Aeroacoustics Conference (33rd AIAA Aeroacoustics Conference)*, 2012. https://doi.org/10.2514/6.2012-2262.

[53] Akkermans, R. A. D., Delfs, J. W., Márquez, C. O., Stuermer, A., Richter, C., Clemen, C., Caruelle, B., and Omais, M., "Aeroacoustic and Aerodynamic Importance of Unequal Rotor Rotation Speeds of a CROR," *New Results in Numerical and Experimental Fluid Mechanics IX*, Vol. 124, 2014. https://doi.org/10.1007/978-3-319-03158-3.

[54] Vaníček, P., "Approximate spectral analysis by least-squares fit - Successive spectral analysis," *Astrophysics and Space Science*, Vol. 4, No. 4, 1969, pp. 387–391. https://doi.org/10.1007/BF00651344.

[55] Vaníček, P., "Further development and properties of the spectral analysis by least-squares," *Astrophysics and Space Science*, Vol. 12, No. 1, 1971, pp. 10–33. https://doi.org/10.1007/BF00656134.

[56] Lummer, M., Richter, C., Proeber, C., and Delfs, J., "Validation of a Model for Open Rotor Noise Predictions and Calculation of Shielding Effects using a Fast BEM," *19th AIAA/CEAS Aeroacoustics Conference*, 2013. https://doi.org/10.2514/6.2013-2096.

[57] Peake, N., and Parry, A. B., "Modern Challenges Facing Turbomachinery Aeroacoustics," *Annual Review of Fluid Mechanics*, Vol. 44, No. 1, 2012, pp. 227–248. https://doi.org/10.1146/annurev-fluid-120710-101231.

[58] Haller, G., "An objective definition of a vortex," *Journal of Fluid Mechanics*, Vol. 525, 2005. https://doi.org/10.1017/S0022112004002526.